

PAPER

# Electronic-structure evolution of $\text{SrFeO}_{3-x}$ during topotactic phase transformation

To cite this article: Jiali Zhao *et al* 2022 *J. Phys.: Condens. Matter* **34** 064001

View the [article online](#) for updates and enhancements.

## You may also like

- [Topotactic reductive synthesis of A-site cation-ordered perovskite  \$\text{YBaCo}\_2\text{O}\_x\$  \( \$x = 4.5-5.5\$ \) epitaxial thin films](#)  
Tsukasa Katayama, Akira Chikamatsu, Tomoteru Fukumura *et al.*
- [Experimental and theoretical investigation of electronic structure of  \$\text{SrFeO}\_{3-x}\text{F}\_x\$  epitaxial thin films prepared via topotactic reaction](#)  
Tsukasa Katayama, Akira Chikamatsu, Hideyuki Kamisaka *et al.*
- [Phase Stability of Nickel Hydroxides and Oxyhydroxides](#)  
A. Van der Ven, D. Morgan, Y. S. Meng *et al.*



**IOP | ebooks™**

Bringing together innovative digital publishing with leading authors from the global scientific community.

Start exploring the collection—download the first chapter of every title for free.

# Electronic-structure evolution of SrFeO<sub>3-x</sub> during topotactic phase transformation

Jiali Zhao<sup>1</sup>, Kaihui Chen<sup>2,3</sup>, Shi-En Li<sup>4</sup>, Qinghua Zhang<sup>1</sup>, Jia-Ou Wang<sup>5</sup>,  
Er-Jia Guo<sup>1,6,7</sup>, Haijie Qian<sup>5</sup>, Lin Gu<sup>1,7</sup> , Tian Qian<sup>1,7</sup>, Kurash Ibrahim<sup>5</sup>,  
Zhen Fan<sup>2,3,\*</sup> and Haizhong Guo<sup>4,8,\*</sup> 

<sup>1</sup> Beijing National Laboratory for Condensed Matter Physics and Institute of Physics, Chinese Academy of Sciences, Beijing 100190, People's Republic of China

<sup>2</sup> Institute for Advanced Materials, South China Academy of Advanced Optoelectronics, South China Normal University, Guangzhou 510006, People's Republic of China

<sup>3</sup> Guangdong Provincial Key Laboratory of Optical Information Materials and Technology, South China Academy of Advanced Optoelectronics, South China Normal University, Guangzhou 510006, People's Republic of China

<sup>4</sup> Key Laboratory of Material Physics, Ministry of Education, School of Physics and Microelectronics, Zhengzhou University, Zhengzhou 450052, People's Republic of China

<sup>5</sup> Institute of High Energy Physics, Chinese Academy of Sciences, Beijing 100049, People's Republic of China

<sup>6</sup> Center of Materials Science and Optoelectronics Engineering, University of Chinese Academy of Sciences, Beijing 100049, People's Republic of China

<sup>7</sup> Songshan Lake Materials Laboratory, Dongguan, Guangdong 523808, People's Republic of China

<sup>8</sup> Collaborative Innovation Center of Light Manipulations and Applications, Shandong Normal University, Jinan 250358, People's Republic of China

E-mail: [fanzhen@m.scnu.edu.cn](mailto:fanzhen@m.scnu.edu.cn) and [hguo@zzu.edu.cn](mailto:hguo@zzu.edu.cn)

Received 18 September 2021, revised 22 October 2021

Accepted for publication 5 November 2021

Published 22 November 2021



CrossMark

## Abstract

Oxygen-vacancy-induced topotactic phase transformation between the ABO<sub>2.5</sub> brownmillerite structure and the ABO<sub>3</sub> perovskite structure attracts ever-increasing attention due to the perspective applications in catalysis, clean energy field, and memristors. However, a detailed investigation of the electronic-structure evolution during the topotactic phase transformation for understanding the underlying mechanism is highly desired. In this work, multiple analytical methods were used to explore evolution of the electronic structure of SrFeO<sub>3-x</sub> thin films during the topotactic phase transformation. The results indicate that the increase in oxygen content induces a new unoccupied state of O 2p character near the Fermi energy, inducing the insulator-to-metal transition. More importantly, the hole states are more likely constrained to the dx<sup>2</sup>-y<sup>2</sup> orbital than to the d3z<sup>2</sup>-r<sup>2</sup> orbital. Our results reveal an unambiguous evolution of the electronic structure of SrFeO<sub>3-x</sub> films during topotactic phase transformation, which is crucial not only for fundamental understanding but also for perspective applications such as solid-state oxide fuel cells, catalysts, and memristor devices.

Keywords: SrFeO<sub>3-x</sub>, topotactic phase transition, electronic structure, x-ray absorption spectroscopy, x-ray resonant photoemission spectroscopy

(Some figures may appear in colour only in the online journal)

\* Authors to whom any correspondence should be addressed.

## 1. Introduction

A rich array of phenomena in transitional-metal (TM) oxides are largely related to oxygen, which pulls electrons away from other atoms in the compounds, resulting in strong electrical fields at the interatomic scale and substantially enhancing correlations between electrons [1]. Recently, oxygen vacancies have come to be seen as an effective degree of freedom to manipulate the properties of TM oxides [2–4]. For example, a topotactic phase transformation between the  $ABO_{2.5}$  brownmillerite (BM) structure and the  $ABO_3$  perovskite (PV) structure is induced by the creation or annihilation of oxygen vacancies [5–14]. The  $ABO_{2.5}$  BM structure emerges from the  $ABO_3$  PV structure by removing one-sixth of the oxygen anions, leaving a structure consisting of alternating layers of corner-sharing  $BO_6$  octahedra and  $BO_4$  tetrahedra. Oxygen vacancy channels form in the tetrahedral layer. They are beneficial to anisotropic transport of ions and also permit oxides to engage in mixed ionic and electronic conduction and catalytic activity, which is useful in numerous practical applications, including solid-state oxide fuel cells, rechargeable batteries, oxygen membranes, gas sensors, and catalysts [5–14]. In addition, a metal-to-insulator transition often occurs during the topotactic phase transformation, which can be exploited in memristor devices [15–19].

While it has been widely reported that the topotactic phase transformation in TM oxides is accompanied by dramatic changes in the physical properties, the underlying mechanism remains poorly understood. The physical properties of the TM oxides are closely related to their electronic structures, such as the TM valence states, the degree of hybridization between the TM  $3d$  and O  $2p$  states, and the band structure near the Fermi energy. Therefore, a detailed investigation of the electronic-structure evolution during the topotactic phase transformation is highly desired for understanding the mechanism underlying such variations in the physical properties.

$SrFeO_{2.5}$  has a BM structure and is an antiferromagnetic insulator. It has a distorted orthorhombic unit cell with lattice constants  $a = 5.672 \text{ \AA}$ ,  $b = 15.59 \text{ \AA}$ , and  $c = 5.527 \text{ \AA}$ , which can be represented by a pseudocubic unit cell with lattice  $a/\sqrt{2} = 4.011 \text{ \AA}$ ,  $b/4 = 3.898 \text{ \AA}$ , and  $c/\sqrt{2} = 3.908 \text{ \AA}$ .  $SrFeO_3$  has a cubic PV structure with a cell parameter of  $3.850 \text{ \AA}$ , helimagnetic order, and metallic conduction.  $SrFeO_{2.5}$  and  $SrFeO_3$  can be transformed from one crystalline phase to the other even at low temperatures because of small Gibbs free-energy difference between the two phases. Density-functional theory calculations show that the formation energy of an oxygen vacancy is rather small for  $SrFeO_3$  ( $\approx 0.4 \text{ eV}$ ) [20] compared with that for  $SrCoO_3$  ( $\approx 1.26 \text{ eV}$ ) [21]. The exotic properties, earth-abundant supply, low cost, and nontoxicity of Fe explain the interest in  $SrFeO_{3-x}$ .

Fan *et al* produced the topotactic phase transformation between  $SrFeO_{2.5}$  and  $SrFeO_3$  by applying an electric field and observed filamentary resistive switching [17]. Khare *et al* used real-time optical spectroscopy to study the same phase transformation, which was produced by annealing in vacuum and in oxygen atmospheres [19]. They reported that  $SrFeO_3$  has negative charge-transfer energy owing to the strong

covalency of the Fe–O bond, which may be the cause of its metallicity during the reversible phase transformation [22]. Bocquet *et al* explored the electronic structure of  $SrFeO_3$  via x-ray photoemission and ultraviolet photoemission spectroscopy of O  $1s$ , Sr  $3d$ , Fe  $2p$ , and Fe  $3s$  core-level states [23]. The results show that the ground state of  $SrFeO_3$  consists of heavily mixed  $d^4$  and  $d^5\bar{L}$  states. Galakhov *et al* investigated the electronic structure of oxygen-deficient ferrites  $SrFeO_{3-x}$  powder ( $x = 0.54, 0.48, 0.32, \text{ and } 0.18$ ) by means of x-ray photoelectron, x-ray emission, and x-ray absorption spectroscopies, and reported that upon increasing the oxygen concentration doped holes become localized in both Fe  $3d$  and O  $2p$  states and the bandgap decreases [24]. Our previous work on the electronic structure evolution from  $SrCoO_{2.5}$  to  $SrCoO_{3-\delta}$  indicates that as the increase of the oxygen content, the hybridization between Co  $3d$  and O  $2p$  is strengthened and the valence band maximum exhibits a typical O  $2p$  characteristic. With further increasing the oxygen content,  $SrCoO_{3-x}$  transform from a high spin  $Co^{3+}$  to an intermediate spin  $Co^{4+}$ , resulting in a transition of insulator to metal [25, 26]. Although these reports and others have explored the various physical properties and the electronic-structure evolution of  $SrFeO_{3-x}$  during the topotactic phase transformation, the orbital configuration near the Fermi edge remains an open question.

The present work uses pulsed laser deposition (PLD) to grow a series of  $SrFeO_{3-x}$  thin films with different oxygen concentrations. The oxygen concentration of  $SrFeO_{3-x}$  ( $0 \leq x \leq 0.5$ ) is tuned during growth under various oxygen pressures. X-ray diffraction (XRD), electric transport measurements, scanning transmission electron microscopy (STEM), x-ray absorption spectroscopy (XAS), x-ray linear dichroism (XLD), and x-ray resonant photoemission spectroscopy (XRPES) are then used to study the evolutions of the structural and electronic properties of  $SrFeO_{3-x}$  driven by oxygen vacancies. The mechanism of the evolutions of the structural and electronic properties were also discussed.

## 2. Experimental

$SrFeO_{2.5}$  (BM-SFO), mixed-phase- $SrFeO_{3-x}$  (Mix-SFO), and  $SrFeO_3$  (PV-SFO) epitaxial thin films ( $\sim 60 \text{ nm}$ ) were deposited on the 40 nm-thick  $SrRuO_3$  bottom electrode layers grown on (001)-oriented  $SrTiO_3$  (STO) substrates by PLD using a KrF excimer laser ( $1.2 \text{ J cm}^{-2}$ ,  $248 \text{ nm}$ ,  $4 \text{ Hz}$ ). Firstly, the  $SrRuO_3$  layers were deposited on the  $SrTiO_3$  substrates at  $680 \text{ }^\circ\text{C}$  and under an oxygen pressure of  $15 \text{ Pa}$ . Subsequently, BM-SFO, Mix-SFO, and PV-SFO thin films were grown at  $660 \text{ }^\circ\text{C}$  and under oxygen partial pressures of  $1, 4, \text{ and } 10 \text{ Pa}$ , respectively. After deposition, the samples were cooled to room temperature at  $10 \text{ }^\circ\text{C min}^{-1}$  under the same oxygen pressure as used during the film growth.

The crystalline structure of the SFO films was characterized by XRD and reciprocal-space mapping (RSM) using a PANalytical X'Pert PRO x-ray diffractometer. XAS, XLD, and XRPES were done at beamline 4B9B of the Beijing Synchrotron Radiation Facility, Institute of High Energy Physics, Chinese Academy of Sciences. The background pressure in the

ultrahigh vacuum chamber was about  $2 \times 10^{-10}$  Torr. The O-K edge and Fe-L edge XAS were recorded in total-electron-yield mode.

### 3. Results and discussion

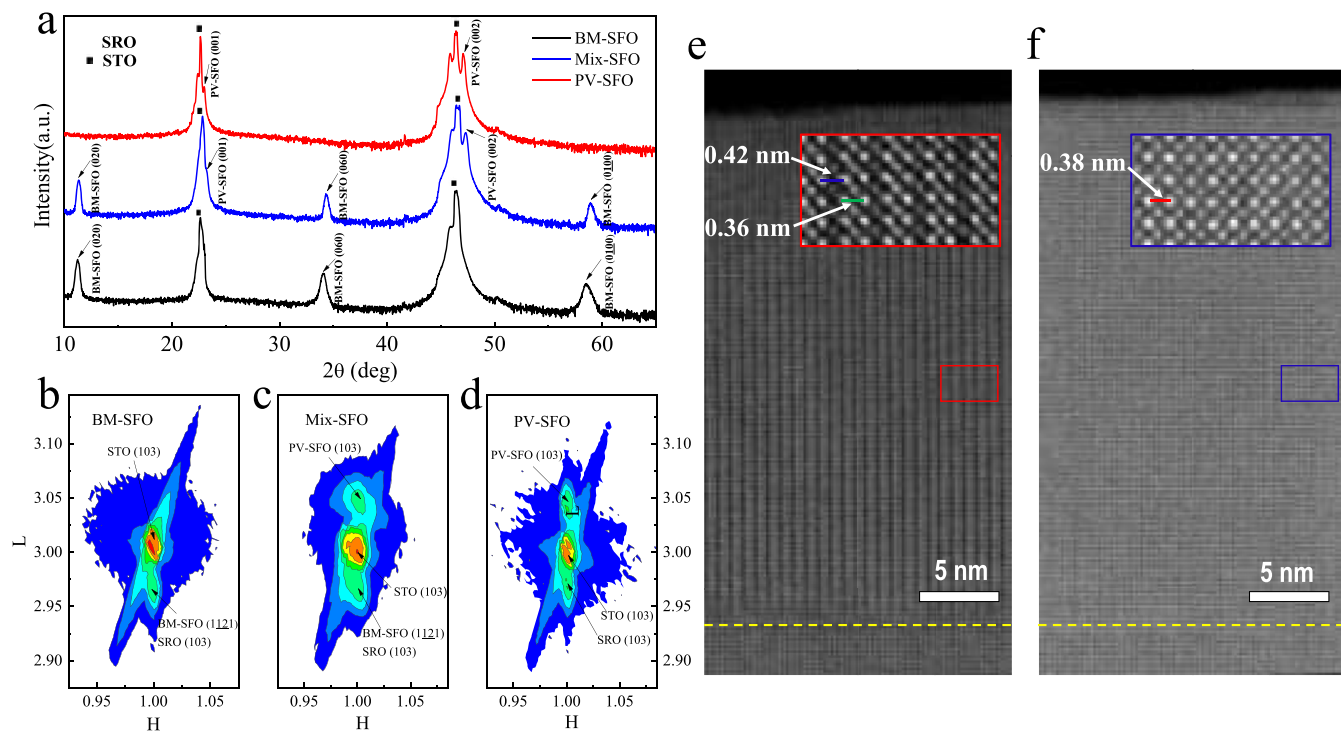
SrFeO<sub>3-x</sub> thin films with various oxygen concentrations were deposited by PLD on SrRuO<sub>3</sub> (SRO)-buffered (001)-oriented STO single crystals. More details on the film growth are given in the experiment section. We used XRD and RSM to characterize the phases of the SrFeO<sub>3-x</sub> films, which are shown in figure 1. Figure 1(a) shows the XRD  $\theta$ - $2\theta$  patterns of the BM-SFO, Mix-SFO, and PV-SFO epitaxial thin films. Half-order reflection peaks are generated by the BM-SFO and Mix-SFO thin films, which is due to the alternate stacking of fully oxygenated octahedral and oxygen-deficient tetrahedral sublayers (e.g., the (020), (060), and (0100) peaks). These peaks are fingerprints of the BM phase. The (040) and (080) peaks of the BM-SFO film overlap with the (001) and (002) peaks of SRO, respectively. Only (00 $l$ ) peaks from the PV phase are generated by the PV-SFO film, confirming its pure PV phase. In addition to the half-order reflection peaks from the Mix-SFO thin film, the PV phase generates the (00 $l$ ) peaks. Therefore, the Mix-SFO thin film should contain both the BM and PV phases. Figure 1(a) confirms that the SrFeO<sub>3-x</sub> thin films fabricated with three different oxygen concentrations contain different phases, which is indicative of a topotactic phase transformation between the BM structure of SrFeO<sub>2.5</sub> and the PV structure of SrFeO<sub>3</sub>. Figures 1(b)–(d) show the RSMs of the three SFO films near the STO (103) Bragg reflection, which indicate that the in-plane lattice of the SFO films and the SRO films are commensurate with the STO substrate. All films coherently grown on the STO substrates are confirmed by RSMs. Moreover, the Mix-SFO thin film generates two resolved peaks indicating a mixture of BM and PV phases, whereas the PV-SFO and BM-SFO films contain pure phases with a single peak in RSM.

STEM is an effective method to directly characterize the microstructure. We measured high-angle annular dark-field (HAADF) STEM of the BM-SFO and PV-SFO thin films, with the results shown in figures 1(e) and (f). Figure 1(e) clearly exhibits periodic dark and bright stripes with different in-plane lattice spacings of 0.42 and 0.36 nm, respectively. The in-plane lattice spacings are consistent with those of the FeO<sub>4</sub> tetrahedral and FeO<sub>6</sub> octahedral layers, respectively, thereby confirming the BM structure. However, the FeO<sub>4</sub> tetrahedral layers, where oxygen vacancies reside, are oriented in the out-of-plane direction, which is inconsistent with the XRD and RSM results that indicating in-plane orientation of the FeO<sub>4</sub> tetrahedral layers. This discrepancy may be due to reordering of the oxygen vacancies occurring during the TEM sample preparation or electron-beam irradiation [27], which may change the orientation of the FeO<sub>4</sub> tetrahedral layers. In contrast, the FeO<sub>4</sub> tetrahedral layers are absent in figure 1(f), where only the FeO<sub>6</sub> octahedral layers are observed. This confirms the pure PV phase in the PV-SFO film.

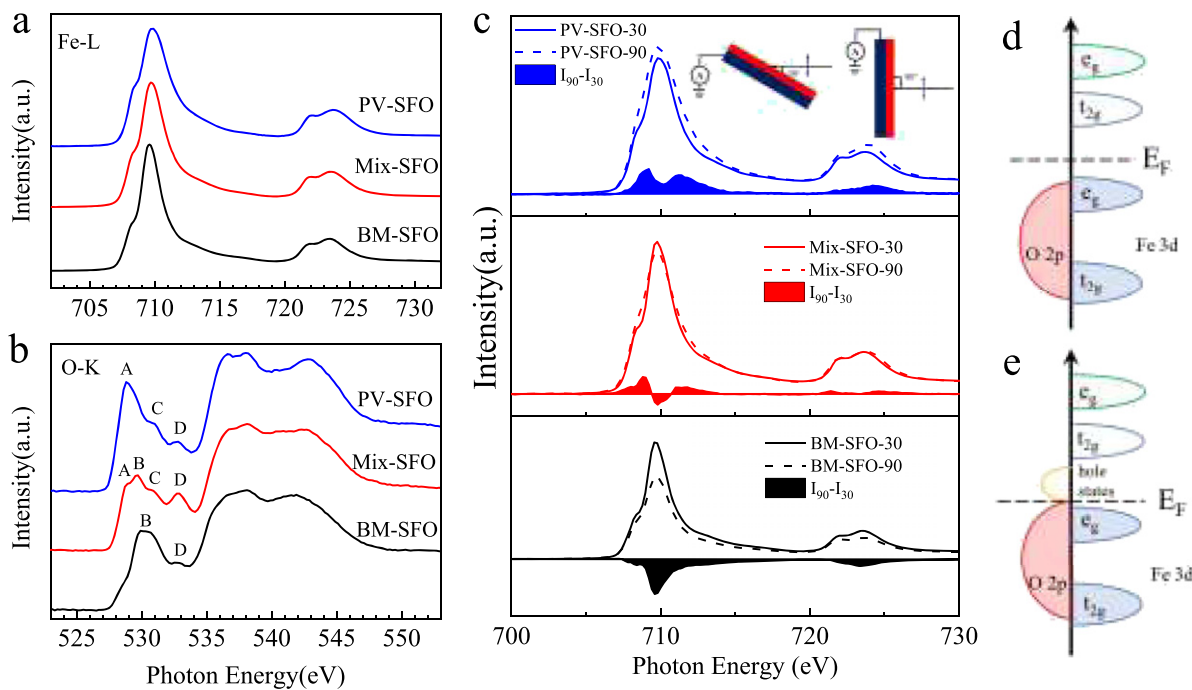
To explore the change of the electronic structure during the topotactic phase transformation between the BM structure of SrFeO<sub>2.5</sub> and the PV structure of SrFeO<sub>3</sub>, we measured XAS, XLD, and resonant photoemission spectroscopy (RPES) of the BM-SFO, Mix-SFO, and PV-SFO films. The XAS of the Fe-L and O-K edges provides information on the unoccupied states. The XAS of the Fe-L edge arises from the transition from Fe 2*p* to Fe 3*d* orbitals. As shown in figure 2(a), the main peaks of the L<sub>3</sub> edge of the BM-SFO, Mix-SFO, and PV-SFO thin films appear at 709.6, 709.7, and 709.8 eV, respectively. From BM-SFO to PV-SFO, the L<sub>3</sub> main peak blueshifts, which means that the valence energy of the Fe ions increases. We detected a small chemical shift between BM-SFO and Mix-SFO, whereas the main peak of PV-SFO broadens. The broader line shape of the main peak of PV-SFO is similar to the signature of the ‘Zhang-Rice singlet’ of the XAS of the Cu-L edge [28–30], suggesting that hole states exist with O 2*p* and Fe 3*d* character owing to the enhanced covalency in the initial state [31]. The ground state of SrFeO<sub>3</sub> consists of heavily mixed *d*<sup>4</sup> and *d*<sup>5</sup> $\underline{L}$  [23].

Figure 2(b) shows the XAS of the O-K edge of the SFO thin films, which originates from the transition from the O 1*s* core-level state to the unoccupied O 2*p* state, thus providing information about the unoccupied O 2*p* states and the hybridization between Fe 3*d* and O 2*p*. In figure 2(b), peak D is observed for all three SFO thin films, which is due to the appearance of the superoxide species O<sub>2</sub><sup>-</sup> that usually exists at film surfaces [25, 32]. The film surface exposed in the atmosphere reacts with substances in the air to form superoxide species. The prepeak A is attributed to transitions to new states of O 2*p* character [24], which means that holes doped in SrFeO<sub>3-x</sub> have partial O 2*p* character. Peaks B and C in the Mix-SFO thin film come from Fe 3*d* *t*<sub>2*g*</sub> and *e*<sub>g</sub> states, respectively. In the PV-SFO thin film, peak C comes from Fe 3*d* *e*<sub>g</sub> states, and the peak from Fe 3*d* *t*<sub>2*g*</sub> states is submerged by peak A due to the splitting of Fe 3*d* *t*<sub>2*g*</sub> and the new states of O 2*p* hole states is too small. Peak B in the BM-SFO thin film does not obviously split, so we assume that either the *t*<sub>2*g*</sub> – *e*<sub>g</sub> splitting is small in BM or the multiplicity of the oxygen sites in BM induces blurs as the results [24]. During the topotactic phase transformation between BM-SFO and PV-SFO, the increase in oxygen content induces new unoccupied states of O 2*p* character near the Fermi energy, which broadens the XAS of the Fe-L edge and causes peak A to emerge in the XAS of the O-K edge.

From the XAS results, we can get the schematic band diagrams of the BM-SFO and PV-SFO thin films, which simply describe the electronic-structure evolution between the topotactic phase transformation of SrFeO<sub>3-x</sub> thin films, shown in figures 2(d) and (e). The we us XLD measurements to get the information of orbital configuration near the Fermi edge. XLD is an ideal technique to investigate the orbital non-occupancy of *dx*<sup>2</sup>-*y*<sup>2</sup> and *d*3*z*<sup>2</sup>-*r*<sup>2</sup> in various TM compounds [30, 33–38]. An x-ray beam perpendicular to the sample surface reflects directly from the *dx*<sup>2</sup>-*y*<sup>2</sup> orbital (*I*<sub>90</sub>) non-occupancy. When the x-ray beam is incident at 30° on the sample surface, the XAS signal contains information from both *dx*<sup>2</sup>-*y*<sup>2</sup> and *d*3*z*<sup>2</sup>-*r*<sup>2</sup> orbitals (*I*<sub>30</sub>). XLD can be calculated simply by *I*<sub>90</sub> – *I*<sub>30</sub>.



**Figure 1.** Crystalline structure of SFO films. (a) XRD  $\theta-2\theta$  patterns of BM-SFO, Mix-SFO, and PV-SFO epitaxial thin films on the SRO-buffered (001)-oriented STO substrates. Reciprocal-space maps around the STO (103) Bragg reflection of three SFO films: (b) BM-SFO, (c) Mix-SFO, and (d) PV-SFO. HAADF STEM images of  $\text{SrFeO}_{3-x}$  thin films of (e) BM-SFO and (f) PV-SFO.



**Figure 2.** XAS of SFO thin films of (a) Fe-L edge and (b) O-K edge. (c) XLD of SFO thin films. Schematic band diagrams of (d) BM-SFO and (e) PV-SFO.

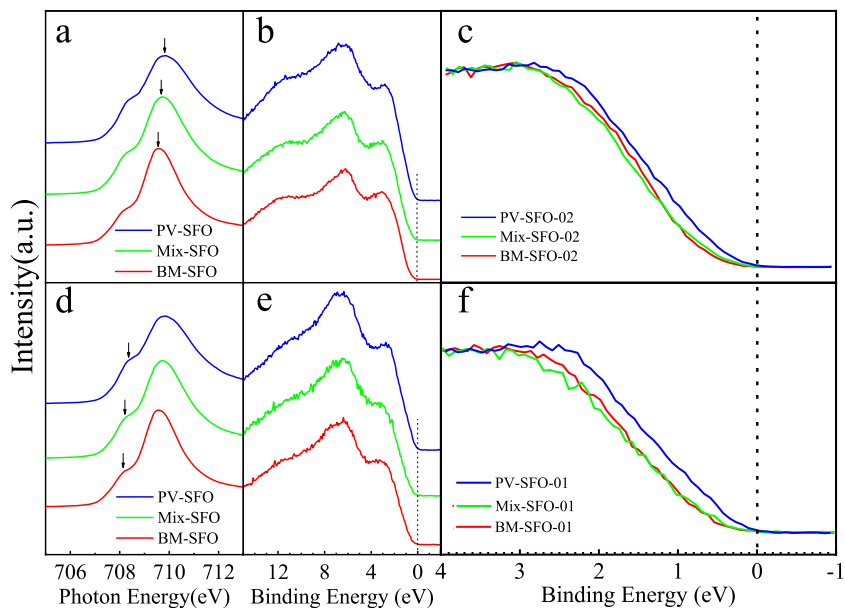


Figure 3. RPES of SFO thin films.

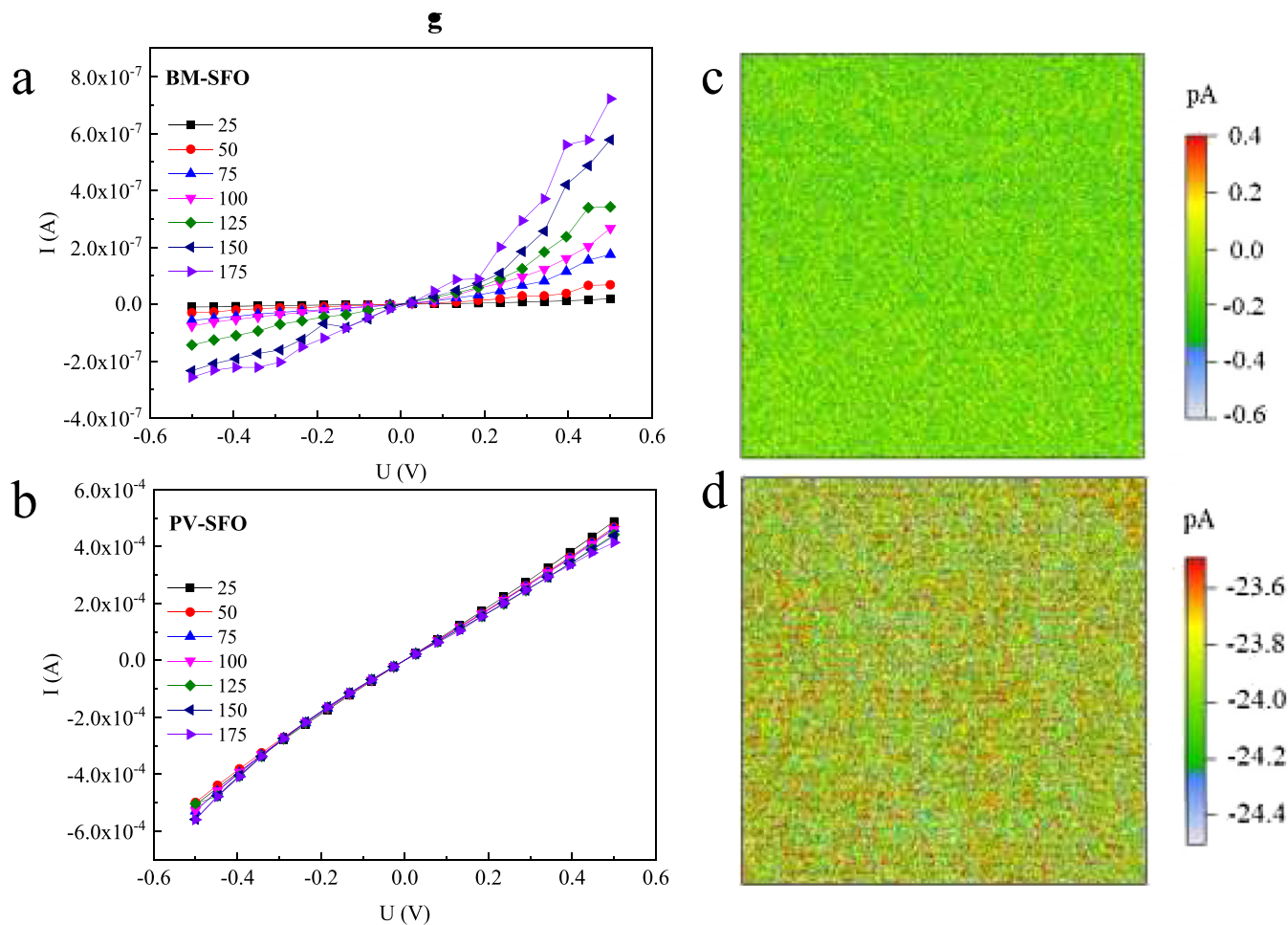


Figure 4.  $I-V$  curves: (a) BM-SFO and (b) PV-SFO. C-AFM current map of a  $5 \times 5 \mu\text{m}^2$  area with  $-0.8 \text{ V}$  applied to SRO bottom electrodes for (c) BM-SFO and (d) PV-SFO.

We use this method to analyze the XLD data of the SFO thin films, as shown in figure 2(c). In the BM-SFO thin film,  $I_{90} - I_{30} < 0$ , which indicates that the unoccupied states from the  $dx^2-y^2$  orbitals are fewer than those of the  $d3z^2-r^2$  orbitals. The opposite result occurs for the PV-SFO thin film, indicating that the hole states are more likely constrained to the  $dx^2-y^2$  orbitals than to the  $d3z^2-r^2$  orbitals. In the BM-SFO thin film, the valence state of Fe is  $Fe^{3+}(e_g^2 t_{2g}^3)$ . The XLD result is determined by the hybridization of O  $2p$  with five  $d$  minor spin orbitals. The closer to O the orbital is, the more it is occupied. The  $dx^2-y^2$  orbital is closer to oxygen than is the  $d3z^2-r^2$  orbital, which means that  $dx^2-y^2$  is more occupied than  $d3z^2-r^2$ , which is consistent with the XLD of BM-SFO. The XLD of the PV-SFO thin film is determined by the hole states of O  $2p$ . The out-of-plane Fe is less hybridized with O  $2p$  than is the in-plane Fe because of the small coordination number.  $dx^2-y^2$  is more hybridized with hole states of O  $2p$  than is  $d3z^2-r^2$ . Therefore, the nonoccupation of the  $dx^2-y^2$  orbital is more than that of the  $d3z^2-r^2$  orbital, which also agrees with the XLD of PV-SFO.

Figure 3 shows the Fe  $2p-3d$  resonant photoemission spectra. To highlight the on-resonance effect, we select two different energies in the Fe- $L_3$  edge, covering the off-resonance and on-resonance photon energy, which are shown in figures 3(d)–(f) and (a)–(c), respectively. The on-resonance photon energy enhances the transition from Fe  $2p$  to Fe  $3d$  and mainly shows the contribution of Fe  $3d$  in the valence band. During the topotactic phase transformation, from off-resonance to on-resonance, no obvious change appears in the valence band near the Fermi energy, which indicates that the increased oxygen content does not substantially change the contribution of Fe  $3d$  states in the valence band. The results of Fe  $2p-3d$  resonant photoemission spectra prove that the increase in oxygen content during the topotactic phase transformation induces new unoccupied states of O  $2p$  character near the Fermi energy once again.

We measured the  $I-V$  curves of the SFO films in the temperature range from 25 to 175 °C to confirm the electrical properties, which are shown in figures 4(a) and (b). With increasing temperature, the resistance of the BM-SFO film decreases, whereas that of the PV-SFO film increases, indicating that the BM-SFO film is an insulator and the PV-SFO film is metallic. Figures 4(c) and (d) show the C-AFM current maps of the BM-SFO and PV-SFO thin films, which were measured with  $-0.8$  V applied to the SRO bottom electrodes. The results show that the PV-SFO thin film carries a much larger current (in magnitude) than does the BM-SFO thin film, which is qualitative evidence that BM-SFO is much more insulating than PV-SFO.

During the topotactic phase transformation, the increase of oxygen content generates a new unoccupied state of O  $2p$  character near the Fermi energy, inducing the insulator-to-metal transition. More importantly, the hole states are more likely constrained to the  $dx^2-y^2$  orbital than to the  $d3z^2-r^2$  orbital. The electronic structure evolution of  $SrFeO_{3-x}$  during the topotactic phase transition is very different with that of  $SrCoO_{3-x}$ . Our previous work on  $SrCoO_{3-x}$  indicates that as the increase of oxygen content, the hybridization between Co

$3d$  and O  $2p$  is strengthened and the valence band maximum exhibits a typical O  $2p$  characteristic, and Co ions in  $SrCoO_{3-x}$  transform from a high spin  $Co^{3+}$  state to an intermediate spin  $Co^{4+}$  state, resulting in a transition of insulator to metal with further increasing oxygen content [25].

## 4. Conclusions

We prepared  $SrFeO_{2.5}$ , mixed- $SrFeO_{3-x}$ , and  $SrFeO_3$  thin films by PLD and demonstrate the topotactic phase transformation along with the insulator-to-metal transition in these films by using XRD, RSM, STEM, and electric transport measurements. To understand the origin behind the insulator-to-metal transition, we further explore the evolution of the electronic structure during the topotactic phase transformation by XAS, XLD, and RPES. The results show that the increase of oxygen content causes new unoccupied states of O  $2p$  character near the Fermi energy, thus inducing the insulator-to-metal transition. More importantly, the hole states in  $SrFeO_3$  thin films are more likely constrained to the  $dx^2-y^2$  orbital than to the  $d3z^2-r^2$  orbital. The results of this work reveal an unambiguous evolution of the electronic structure of  $SrFeO_{3-x}$  single crystalline film during topotactic phase transformation, which is vital not only for fundamental research but also for applications such as solid-state oxide fuel cells, catalysts, and memristor devices.

## Acknowledgments

This work was supported by the National Natural Science Foundation of China (Grant Nos. U1932125, 12005252 and 12174347), the Program for the Innovation Team of Science and Technology at the University of Henan (No. 20IRT-STHN014), Excellent Youth Foundation of Henan Scientific Committee (No. 202300410356), the CAS Interdisciplinary Innovation Team (No. JCTD-2019-01), and the Science and Technology Program of Guangzhou (No. 2019050001).

## Data availability statement

The data generated and/or analysed during the current study are not publicly available for legal/ethical reasons but are available from the corresponding author on reasonable request.

## ORCID iDs

Lin Gu  <https://orcid.org/0000-0002-7504-031X>  
Haizhong Guo  <https://orcid.org/0000-0002-6128-4225>

## References

- [1] Heber J 2009 *Nature* **459** 28–30
- [2] Kalinin S V and Spaldin N A 2013 *Science* **341** 858–9
- [3] Guo H et al 2016 *Adv. Mater. Interfaces* **3** 1500753
- [4] Gao Z, Huang X, Li P, Wang L, Wei L, Zhang W and Guo H 2018 *Adv. Mater. Interfaces* **5** 1701565

- [5] Jeon H, Bi Z, Choi W S, Chisholm M F, Bridges C A, Paranthaman M P and Lee H N 2013 *Adv. Mater.* **25** 6459–63
- [6] Huang S, Feng S, Lu Q, Li Y, Wang H and Wang C 2014 *J. Power Sources* **251** 357–62
- [7] Kim Y M *et al* 2012 *Nat. Mater.* **11** 888–94
- [8] Sengodan S, Choi S, Jun A, Shin T H, Ju Y-W, Jeong H Y, Shin J, Irvine J T S and Kim G 2015 *Nat. Mater.* **14** 205–9
- [9] Auckett J E, Studer A J, Pellegrini E, Ollivier J, Johnson M R, Schober H, Müller W and Ling C D 2013 *Chem. Mater.* **25** 3080–7
- [10] Paulus W *et al* 2008 *J. Am. Chem. Soc.* **130** 16080–5
- [11] Acharya S K *et al* 2016 *ACS Appl. Mater. Interfaces* **8** 7902–11
- [12] Tambunan O T *et al* 2014 *Appl. Phys. Lett.* **105** 063507
- [13] Acharya S K *et al* 2017 *Nanoscale* **9** 10502–10
- [14] Wang X S *et al* 2020 *Sci. China: Phys., Mech. Astron.* **63** 297011
- [15] Nallagatla V R, Kim J, Lee K, Chae S C, Hwang C S and Jung C U 2020 *ACS Appl. Mater. Interfaces* **12** 41740–8
- [16] Tian J *et al* 2020 *ACS Appl. Mater. Interfaces* **12** 21883–93
- [17] Tian J *et al* 2019 *Adv. Mater.* **31** 1903679
- [18] Cao T *et al* 2020 *J. Phys. D: Appl. Phys.* **53** 424001
- [19] Rao J *et al* 2021 *Mater. Today Phys.* **18** 100392
- [20] Das T, Nicholas J D and Qi Y 2017 *J. Mater. Chem. A* **5** 4493–506
- [21] Tahini H A, Tan X, Schwingenschlögl U and Smith S C 2016 *ACS Catal.* **6** 5565–70
- [22] Khare A *et al* 2017 *Adv. Mater.* **29** 1606566
- [23] Bocquet A E, Fujimori A, Mizokawa T, Saitoh T, Namatame H, Suga S, Kimizuka N, Takeda Y and Takano M 1992 *Phys. Rev. B* **45** 1561–70
- [24] Galakhov V R, Kurmaev E Z, Kuepper K, Neumann M, McLeod J A, Moewes A, Leonidov I A and Kozhevnikov V L 2010 *J. Phys. Chem. C* **114** 5154–9
- [25] Zhao J *et al* 2019 *Sci. China Mater.* **62** 1162–8
- [26] Zhang B *et al* 2019 *Phys. Rev. B* **100** 144201
- [27] Wang L, Yang Z, Bowden M E and Du Y 2019 *Appl. Phys. Lett.* **114** 231602
- [28] Li W M *et al* 2019 *Proc. Natl Acad. Sci. USA* **116** 12156–60
- [29] Chen Y J *et al* 2013 *Phys. Rev. B* **88** 134525
- [30] Chakhalian J, Freeland J W, Habermeier H-U, Cristiani G, Khaliullin G, van Veenendaal M and Keimer B 2007 *Science* **318** 1114–7
- [31] Abbate M *et al* 1992 *Phys. Rev. B* **46** 4511–9
- [32] Karvonen L, Valkeapää M, Liu R-S, Chen J-M, Yamauchi H and Karppinen M 2010 *Chem. Mater.* **22** 70–6
- [33] Guo E J, Desautels R D, Keavney D, Herklotz A, Zac Ward T, Fitzsimmons M R and Lee H N 2019 *Phys. Rev. Mater.* **3** 014407
- [34] Liao Z *et al* 2019 *Nat. Commun.* **10** 589
- [35] Guo E J *et al* 2019 *Sci. Adv.* **5** eaav5050
- [36] Jin Q *et al* 2020 *Adv. Mater.* **33** 2005920
- [37] Li S *et al* 2020 *Adv. Mater.* **33** 2001324
- [38] Chen S *et al* 2021 *Sci. China: Phys., Mech. Astron.* **64** 287711